

Geometry and growth contributions to cosmic shear observables

José Manuel Zorrilla Matilla,^{1,*} Zoltán Haiman,¹ Andrea Petri,² and Toshiya Namikawa^{3,4}

¹*Department of Astronomy, Columbia University, New York, NY 10027, USA*

²*Department of Physics, Columbia University, New York, NY 10027, USA*

³*Department of Physics, Stanford University, Stanford, California 94305, USA*

⁴*Kavli Institute for Particle Astrophysics and Cosmology, SLAC National Accelerator Laboratory, 2575 Sand Hill Road, Menlo Park, California 94025, USA*

(Dated: October 13, 2018)

We explore the sensitivity of weak lensing observables to the expansion history of the Universe and to the growth of cosmic structures, as well as the relative contribution of both effects to constraining cosmological parameters. We utilize ray-tracing dark-matter-only N-body simulations and validate our technique by comparing our results for the convergence power spectrum with analytic results from past studies. We then extend our analysis to non-Gaussian observables which cannot be easily treated analytically. We study the convergence (equilateral) bispectrum and two topological observables, lensing peaks and Minkowski functionals, focusing on their sensitivity to the matter density Ω_m and the dark energy equation of state w . We find that a cancellation between the geometry and growth effects is a common feature for all observables, and exists at the map level. It weakens the overall sensitivity by up to a factor of 3 and 1.5 for w and Ω_m , respectively, with the bispectrum worst affected. However, combining geometry and growth information alleviates the degeneracy between Ω_m and w from either effect alone. As a result, the magnitude of marginalized errors remain similar to those obtained from growth-only effects, but with the correlation between the two parameters switching sign. These results shed light on the origin of cosmology-sensitivity of non-Gaussian statistics, and should be useful in optimizing combinations of observables.

Keywords: Weak Gravitational Lensing

I. INTRODUCTION

A cosmological model with a nearly scale-invariant primordial fluctuation spectrum, cold dark matter (CDM) and dark energy (DE) matches well a wide range of observations, from the Universe’s expansion measured by standard candles [1, 2] and standard rulers [3], to its primordial chemical composition [4, 5], structure formation and the properties of the Cosmic Microwave Background (CMB) [6]. While non-baryonic DM and DE make up most of the present-day energy density of the Universe [7], the nature of either dark component remains unclear.

Cosmic shear is the weak gravitational lensing of background sources by large scale structure [8, 9]. It probes the matter density field through the gravitational potential fluctuations, and is also sensitive to the expansion history of the Universe through the distances between the observer, lensed source and lensing structures. While lensing is usually characterized by a measurement of the shear through the shapes of background galaxies, convergence (magnification) statistics can be inferred from these measurements, and are considered here for ease of computation. The polyspectra of the convergence field are equal to the E-modes of the shear field.

Ongoing and upcoming surveys, such as the Dark Energy Survey (DES [10]), the Large Synoptic Survey Telescope (LSST [11]), the Euclid mission [12] and the Wide Field Infrared Survey Telescope (WFIRST [13]), include

weak lensing in their scientific program as part of their effort to test the concordance model with unprecedented precision and shed light on the nature of DM and DE. To realize this potential, we need observables that extract all the cosmological information from the data, as well as models capable of predicting them with high accuracy.

Second-order statistics do not fully capture non-Gaussianities in the lensing signal from non-linear gravitational collapse on small scales. Numerous alternative observables have been proposed to extract this extra information, from higher-order correlation functions [14, 15] and moments [16] to topological features like local maxima (peaks) [17] and Minkowski functionals [18].

In this work, our goal is to clarify the sensitivity of such observables to the expansion history of the Universe (“geometry”) and to the evolution of primordial inhomogeneities into cosmic structures (“growth”). The analogous question has been addressed for the convergence (κ) power spectrum [19]. The geometry *vs.* growth decomposition of the power spectrum has improved our understanding of constraints on DE from weak lensing [20], provided an alternative cosmological probe independent of the growth of structures [21, 22], has been used to strongly constrain deviations from general relativity [23] and has allowed a consistency test of the standard cosmological model [24].

Our work extends previous studies to observables beyond the power spectrum. In particular, we analyze the equilateral bispectrum and two simple but promising topological observables: lensing peaks and Minkowski functionals. We restrict our analysis to two parameters that can influence lensing observables significantly

* jzorrilla@astro.columbia.edu

TABLE I. Parameters of the eight models explored around the fiducial model ($\Omega_m = 0.26$, $w = -1.0$). All models are spatially flat with $\Omega_\Lambda = 1 - \Omega_m$ and consider a constant equation of state parameter w for DE.

Ω_m	w	Ω_m	w
0.20	-1.0	0.26	-0.5
0.23	-1.0	0.26	-0.8
0.29	-1.0	0.26	-1.2
0.32	-1.0	0.26	-1.5

through both geometry and growth: the total matter density (Ω_m) and the DE equation of state as parametrized with a constant ratio of its pressure to its energy density (w). Future work should include a full cosmological parameter set. We disentangle the two contributions by measuring observables over a collection of mock κ maps built from ray-tracing N-body simulations.

The paper is organized as follows. In § II, we describe the suite of simulations we used and our method to separate the effects of geometry and growth on the observables. In § III, we show the sensitivity of each observable to both Ω_m and w , discussing the separate contributions from geometry and growth, and in § IV we show how they impact parameter inference. We then discuss our results in § V and summarize our conclusions in § VI.

II. DISENTANGLING GEOMETRY FROM GROWTH IN SIMULATIONS

We measured lensing observables on mock κ maps generated for 9 flat Λ CDM cosmologies. We considered only DE models with a constant ratio of pressure to energy density (w). Apart from w , we also varied Ω_m , with a fiducial model corresponding to $\{\Omega_m, w\} = \{0.26, -1.0\}$ and the remaining 8 cosmologies each differing from it in just one parameter (see Table I). For all models, we fixed the amplitude of perturbations at $\sigma_8=0.8$, the Hubble constant to $h = 0.72$, the spectral index to $n_s=0.96$ and the effective number of relativistic degrees of freedom to $N_{\text{eff}} = 3.04$.

A. Simulating weak lensing maps

A set of mock convergence maps was generated by ray-tracing through the outputs of dark matter-only N-body simulations, following the multiple lens plane algorithm implemented in LENSTOOLS. We used full ray-tracing to avoid any potential bias in the convergence descriptors under study. While it has been shown that the Born approximation is accurate for the galaxy lensing power spectrum [25] and bispectrum [26], it can introduce significant biases for higher-order moments [27] and its effects on topological descriptors are yet unclear. We give

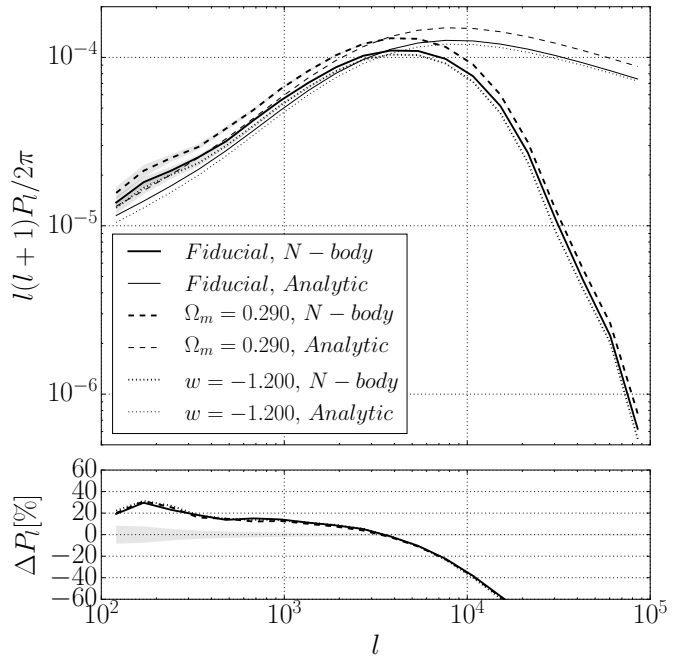


FIG. 1. Comparison between the power spectra measured for selected models, as labeled, over noiseless, un-smoothed κ maps (thick lines) and analytic predictions using a fitting formula [31] for the matter power spectrum (thin lines). Percent differences between measured and predicted power spectra are depicted in the lower panel. Shaded areas represent ± 1 standard deviations around the average, scaled to a 1000 deg^2 survey, and in the lower panel only the standard deviation for the fiducial model is plotted for reference.

a brief outline of our simulation pipeline here, and refer readers for a detailed description in [28].

The observer’s past light cone is discretized in a set of lens planes separated by a constant comoving distance of $80 h^{-1} \text{ Mpc}$. For each cosmology, we evolved the matter density field in a single box of side $240 h^{-1} \text{ Mpc}$, which can cover a field of view of $3.5 \times 3.5 \text{ deg}^2$ up to a redshift $z \approx 3$. The N-body simulations were run using GADGET2 [29] with the same initial conditions. Each box contains 512^3 particles, yielding a mass resolution of $\approx 10^{10} M_\odot$. All simulation volumes were randomly shifted and rotated to generate 1024 different κ maps for each cosmology. This is justified by previous work [30], which has shown that a single N-body simulation can be recycled to generate as many as $\approx 10^4$ statistically independent realizations of the projected 2D convergence field.

Bundles of 1024×1024 uniformly distributed rays were traced back to the lensed galaxies’ redshift and the convergence was reconstructed from the accumulated deflection of the rays by the discrete lens planes. For simplicity, we assumed all source galaxies are uniformly distributed at a single redshifts, chosen to be either $z_s = 1$ or $z_s = 2$.

We included the effect of galaxy shape noise assuming it is uncorrelated with the lensing signal and its probabil-

ity distribution function (PDF) is a Gaussian with zero mean. The variance of the shape noise depends on the r.m.s. intrinsic ellipticity noise (σ_ϵ), the source galaxy surface density (n_{gal}) and the pixel size (θ_p), as [32]

$$\sigma_p^2 = \frac{\sigma_\epsilon^2}{2n_{gal}\theta_p}. \quad (1)$$

For this work we considered an intrinsic ellipticity noise of $\sigma_\epsilon = 0.4$ and a galaxy density of $n_{gal} = 25 \text{ arcmin}^{-1}$, similar to the expectation for LSST but conservative compared to the galaxy densities expected in deeper surveys, such as Euclid and WFIRST. We generated a single set of 1024 noise-only maps and added them to the noiseless κ maps ray-traced from the N-body simulations. We smoothed the noiseless κ and shape noise maps with the same 2D Gaussian kernel,

$$W(\theta) = \frac{1}{2\pi\theta_S^2} \exp\left[-\frac{\theta^2}{2\theta_S^2}\right], \quad (2)$$

with θ the angular distance to each pixel, and a characteristic width $\theta_S = 1 \text{ arcmin}$. In this analysis we did not combine different smoothing scales. The smoothing suppresses power on small scales corresponding to spherical multipoles on the sky $\ell \gtrsim 12000$, which corresponds to the scale at which we are still not limited by the finite resolution of our simulations (see Fig.1). We do not show results beyond $l = 10000$, and the topological features, measured on the smoothed maps, do not contain information from smaller scales.

B. Isolating the effect of geometry vs. growth

Galaxy shape distortions by gravitational lensing result from the convolution of the lens properties and the

distances between source galaxies, lenses and the observer. Both effects depend on cosmology; the former through the evolution of mass inhomogeneities, and the latter through the expansion history of the Universe. To account for these effects separately in our simulations, we evolved the matter density field according to a cosmological model, but during the ray-tracing, we allowed distances to correspond to a different cosmology.

In our implementation of the multi-plane algorithm, lens planes are located at the same comoving distances from the observer for all models and we disentangled growth and geometry by modifying the lens planes' properties.

The lensing potential for a lens at a comoving distance of χ_i , given a set of cosmological parameters \mathbf{p} , is determined by its mass surface density,

$$\Sigma_i(x, y; \mathbf{p}) = \frac{3H_0^2\Delta}{2c^2} \frac{\chi_i}{a(\chi_i, \mathbf{p})} \delta\Omega_m(x, y; z(\chi_i, \mathbf{p}); \mathbf{p}), \quad (3)$$

where (x, y) are angular positions on the lens plane, Δ is the plane's thickness ($80 h^{-1} \text{ Mpc}$), χ the comoving distance, a the scale factor and $\delta\Omega_m$ the product of the density contrast and the matter density parameter. The sensitivity of an observable to cosmology refers to the change in that observable for a set of parameters \mathbf{p} relative to the same observable for a fiducial model \mathbf{p}_0 .

The effect of geometry can be estimated by evolving the perturbations according to \mathbf{p}_0 and evaluating them at redshift $z(\chi_i, \mathbf{p})$, keeping the geometrical prefactor χ/a equal to the value that corresponds to the cosmological model \mathbf{p} . Conversely, the effect of the growth of structures can be captured by keeping the geometrical prefactor equal to its value in the fiducial model and evaluating the density perturbations at $z(\chi_i, \mathbf{p}_0)$ after evolving them according to \mathbf{p} .

$$\Sigma_i^{Geometry}(x, y; \mathbf{p}; \mathbf{p}_0) = \frac{3H_0^2\Delta}{2c^2} \frac{\chi_i}{a(\chi_i, \mathbf{p})} \delta\Omega_m(x, y; z(\chi_i, \mathbf{p}); \mathbf{p}_0) \quad (4)$$

$$\Sigma_i^{Growth}(x, y; \mathbf{p}; \mathbf{p}_0) = \frac{3H_0^2\Delta}{2c^2} \frac{\chi_i}{a(\chi_i, \mathbf{p}_0)} \delta\Omega_m(x, y; z(\chi_i, \mathbf{p}_0); \mathbf{p}) \quad (5)$$

This approach does not require running separate N-body simulations to generate growth-only and geometry-only convergence maps, but it involves saving additional GADGET2 snapshots, since fixed comoving distances correspond to different scale factors for different cosmologies. For each model \mathbf{p} , additional snapshots at redshifts $z(\chi_i, \mathbf{p}_0)$ are needed. For the fiducial cosmology, we saved additional snapshots at redshifts $z_k(\chi_i, \mathbf{p}_k)$ for each \mathbf{p}_k model considered.

III. SENSITIVITY TO Ω_m AND w

The percentage deviation of an observable relative to its value in the fiducial model measures its sensitivity to changes in cosmology. For galaxy lensing, we are interested in observables measured over κ maps that include shape noise. We focus on the behavior of four observables: the power spectrum, which has already been studied analytically and will serve as a test of our simulation-

based approach, the equilateral bispectrum, which should be zero for a Gaussian random field, and two topological features that have been used to probe non-Gaussianities: lensing peaks and Minkowski functionals. We measured the sensitivities from the full ray-traced N-body simulations, as well as from simulations that only capture the changes due to either the expansion history or to the structure growth in a given cosmology.

A. Power spectrum

The convergence power spectrum is the Fourier transform of the 2-point correlation function of $\kappa(x, y)$ and is one of the most popular weak lensing observables. For a flat cosmology, with lensed sources at a fixed redshift, and using the Limber and flat-sky approximations, the power spectrum can be expressed as a line-of-sight integral of the matter power spectrum, weighted by a geometrical kernel [33]

$$P_k(l) = \frac{9}{4} \left(\frac{H_0}{c} \right)^4 \Omega_m^2 \int_0^{\chi_s} \frac{d\chi}{a^2(\chi)} \left(1 - \frac{\chi}{\chi_s} \right)^2 P_\delta \left(\frac{l}{\chi}; \chi \right) \quad (6)$$

Where χ is the comoving distance and χ_s the comoving distance to the lensed galaxies. Geometry affects the power spectrum through χ and the scale factor a . Growth enters the above expression through the matter power spectrum, P_δ (including non-linear effects), and the Ω_m^2 outside of the integral. For our analytic calculations, we used the NICAEA implementation of the convergence power spectrum with the prescription from [31] for the matter power spectrum.

We determined the percentage deviation of the power spectrum relative to the fiducial cosmology over 1024 noiseless, un-smoothed κ maps for each non-fiducial cosmology, and compared the results with analytic predictions. These results, shown in the upper panels of Fig. 2, match the analytic predictions within the statistical uncertainties, and are also in good agreement with the findings of [19]. The sensitivity is only weakly dependent on the multipole.

The sensitivity to Ω_m is dominated by growth, with a $\approx 25\%$ change that is what would be expected from the $\approx 12\%$ change in Ω_m (Ω_m^2 outside the integral in Eq. 6). Geometry acts in the opposite direction, reducing the overall sensitivity by $\approx 20\%$. The sensitivity to w is dominated by geometry. While we expected its sensitivity to be smaller than that to Ω_m due to the integrating effect, the partial cancellation between growth and geometry is even more severe. It reduces the sensitivity further ($\approx 50\%$) to a level of $\approx 5\%$ for a 20% change in the parameter. The smaller sensitivity should propagate into tighter constraints on Ω_m than on w from weak lensing data.

The origin of the partial cancellation is explained in detail in [19], but we reproduce the argument here for convenience. Making w more negative, from the fiducial

$w = -1.0$ to -1.2 , yields a higher DE density in the past. The comoving distance to the source galaxies' redshift becomes larger, and so does the cumulative effect of small deflections experienced by light rays. As a result, the effect due to geometry is an increase of the lensing signal. Since we fix the amplitude of the perturbations at the present time (σ_8) in our simulations, a higher DE density in the past means there are fewer structures to deflect the light rays in the past, and the growth contribution to the lensing signal is smaller compared to a model with constant dark matter density.

Galaxy shape noise introduces a scale-dependence to the relative sensitivity, as clearly seen in the lower panels of Fig. 2. At small scales, white noise dominates the power spectrum and suppresses its sensitivity to cosmological parameters. Galaxy shape noise then limits the information that can be extracted from the convergence power spectrum at small scales.

B. Equilateral bispectrum

The natural extension to the two-point correlation function is the three-point correlation function, or its Fourier transform, the bispectrum. A non-zero bispectrum is a clear non-Gaussian signal and has been detected in shear data [34, 35]. The analog of Eq. (6) links the convergence bispectrum to the bispectrum of the underlying matter density field through a Limber integration [33]

$$\mathbf{B}_k(\mathbf{l}_1, \mathbf{l}_2, \mathbf{l}_3) = \frac{27}{8} \left(\frac{H_0}{c} \right)^6 \Omega_m^3 \int_0^{\chi_s} \frac{d\chi}{(\chi a(\chi))^3} \left(1 - \frac{\chi}{\chi_s} \right)^3 \delta^D(\mathbf{l}_1 + \mathbf{l}_2 + \mathbf{l}_3) \mathbf{B}_\delta \left(\frac{\mathbf{l}_1}{\chi}, \frac{\mathbf{l}_2}{\chi}, \frac{\mathbf{l}_3}{\chi}; \chi \right) \quad (7)$$

Where δ^D is a Dirac delta. When the lengths of the triangle defined by the three points on which the correlation function are measured are the same, the result is the equilateral bispectrum (\mathbf{B}_{III}). In an exercise analogous to the one done for the power spectrum, we measured \mathbf{B}_{III} for our mock noiseless convergence maps and show their relative sensitivity to the cosmological parameters in Fig. 3.

While noisier, the parameter-sensitivity has a behavior very similar to the case of the power spectrum, in terms of its weak dependence on the angular scale ℓ , order of magnitude, and split between geometry and growth. The most noticeable difference is that the cancellation between both effects is almost perfect for w , resulting in a statistic that is almost insensitive to that parameter. The results for the lensed galaxies at $z_s = 2$ are similar, and show the same cancellation for w . The addition of shape noise results in an even noisier measurement (see §IV) with error bars 3-4 times larger than the ones displayed in Fig. 3 for the noiseless case. There is no average sensitivity suppression at small scales, because the shape noise is Gaussian.

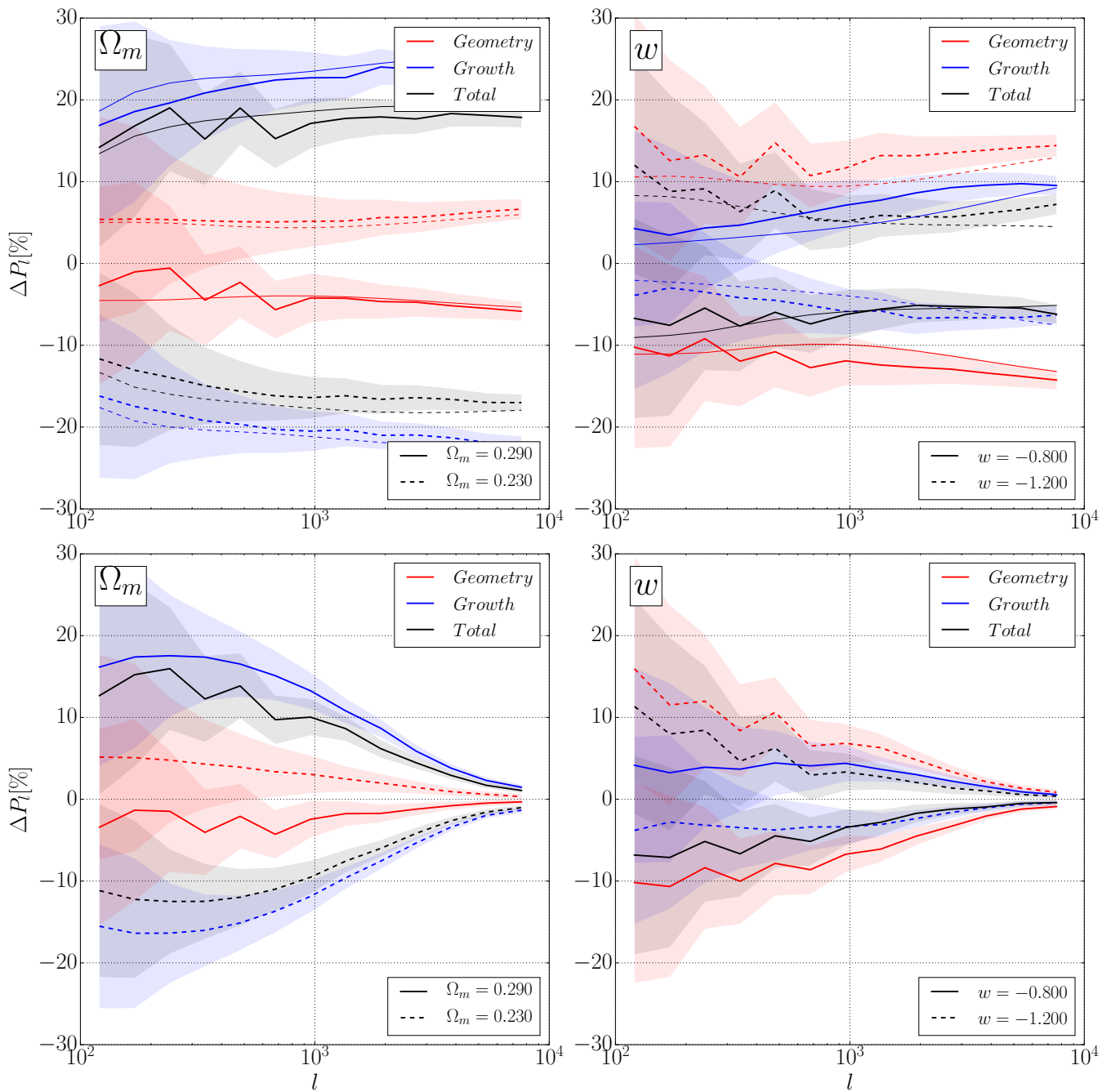


FIG. 2. (color online) Sensitivity of the power spectrum to Ω_m and w for noiseless (upper panels) and noisy (lower panels) convergence. Estimates including only geometry effects are shown in red, those including only growth effects in blue, and those including both effects in black. In the upper panels, analytic predictions are displayed with thin lines, for comparison. Source galaxies are at $z_s = 1.0$ in all cases. Shaded areas represent a ± 1 standard deviation around the measured averages scaled to a survey sky coverage of 1000 deg^2 and only selected models are displayed for clarity.

C. Lensing peaks

Peaks, defined as local maxima on smoothed κ maps, probe high-density regions, where non-Gaussianities of the convergence should be enhanced. Also, they are

computationally inexpensive to measure, making them an attractive observable to combine with others for cosmological inference. Indeed, their distribution as a function of their height, or peak function, has been forecast to improve constraints obtained using only second-order

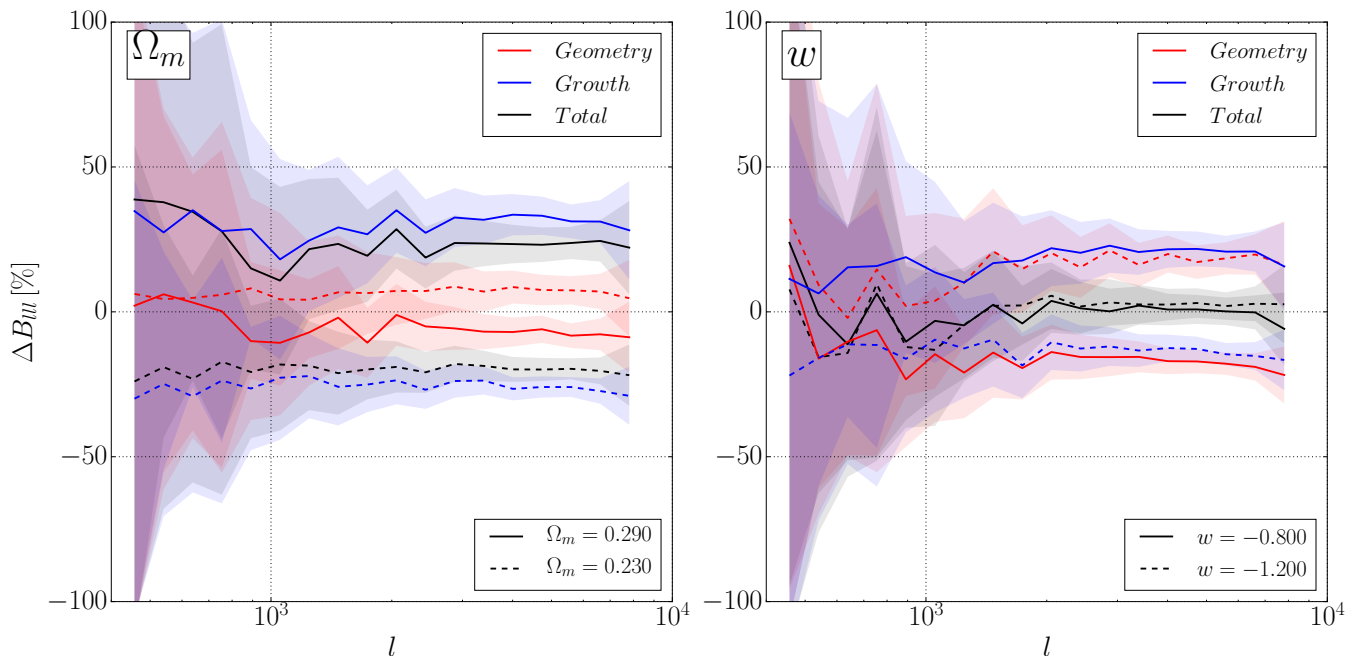


FIG. 3. (color online) *Sensitivity of the equilateral bispectrum of the noiseless convergence field to Ω_m and w . Both panels show the percentage deviation in each model from the fiducial bispectrum. For clarity, only two models are depicted per panel, with the source galaxies at $z_s = 1$. As in Fig. 2, black lines show the net sensitivity, red lines the sensitivity due only to differences in geometry and blue lines the sensitivity due only to differences in growth. Shaded areas represent ± 1 standard deviation around the measured averages, scaled to a 1000 deg^2 survey.*

statistics by a factor of 2–3 [36, 37]. Similar improvements have now been found in recent lensing survey data [38–40].

We extracted peak catalogues from our mock convergence maps and computed the percentage deviation of the peak height function relative to the fiducial model. The results for the noisy case are shown in Fig. 4. We again observe some similarities between the sensitivity of the peak height functions and that of the power spectrum. The Ω_m -sensitivity is dominated by growth, while geometry dominates the sensitivity to w . There is also a partial cancellation between the two effects, and the cancellation is stronger for w , yielding a reduced net sensitivity compared to Ω_m , by a factor of ≈ 2 .

For high peaks, the sign of the parameter-sensitivity is the same as for the power spectrum, but the sign reverses for low peaks, whose abundance is anti-correlated with those of high peaks. High peaks are $\approx 2 - 3$ times more sensitive than low peaks, but there are fewer of them to help discern between models (see §V). Shape noise modifies the peak function, by introducing new peaks, eliminating some, and spreading the height of those that survive from the noiseless maps. As a result, it reduces the sensitivity by a factor of ≈ 2 , especially for the noise-dominated low peaks, and moves the turn-over point, where the parameter-sensitivity changes sign, from $\mathcal{S}/\mathcal{N} \approx 1$ for noiseless κ to $\mathcal{S}/\mathcal{N} \approx 2.5$ (\mathcal{S}/\mathcal{N} is the height of the peaks expressed in units of σ_{noise}).

For noisy κ and lensed galaxies at $z_s = 2$, the turn-over point moves to even higher κ , from $\mathcal{S}/\mathcal{N} \approx 2.5$ to ≈ 3 , and the relative sensitivity of low peaks increases by a factor of ≈ 2 , while the sensitivity of high peaks remains the same.

D. Minkowski functionals

Minkowski functionals (MFs) on 2D fields are topological measures on iso-contours [41]. They capture statistical information of all orders and have been shown to constrain cosmology, improving errors computed exclusively from the power spectrum, in theoretical studies [42] and also when applied to observations [43, 44].

The three MFs on a 2D map measure the area (V_0), boundary length (V_1) and the Euler characteristic (V_2) of the set of points where the value of the function exceeds a pre-specified threshold (κ_{th}):

$$V_0(\kappa_{th}) = \frac{1}{A} \int_{\Sigma(\kappa_{th})} da, \quad (8)$$

$$V_1(\kappa_{th}) = \frac{1}{4A} \int_{\partial\Sigma(\kappa_{th})} dl, \quad (9)$$

$$V_2(\kappa_{th}) = \frac{1}{2\pi A} \int_{\partial\Sigma(\kappa_{th})} \kappa dl, \quad (10)$$

where A is the total area of the map, $\Sigma(\kappa_{th})$ is the set

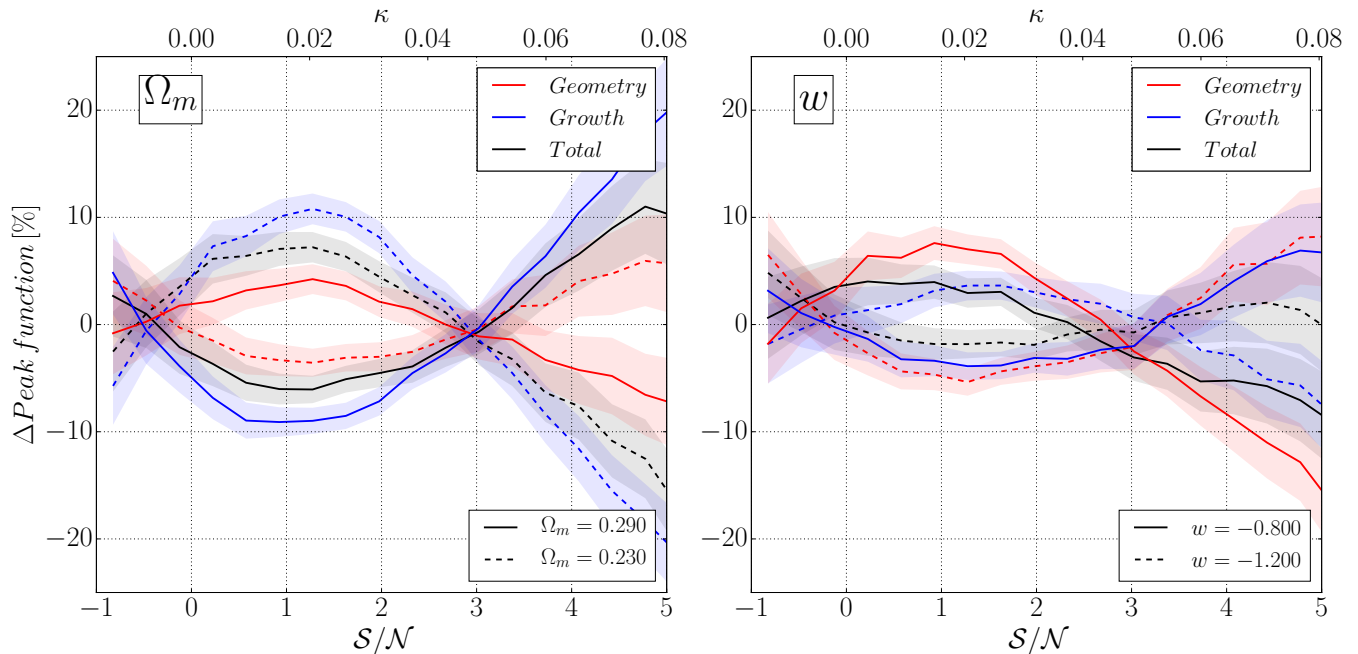


FIG. 4. (color online) Sensitivity of peak counts to Ω_m and w on noisy convergence maps. Both panels show the percentage difference between the peak counts in a given cosmology and in the fiducial model. Peak height is expressed in units of κ and in units of σ_{noise} , S/N . For clarity, only two models are depicted per panel, with source galaxies at $z_s = 1$. The color scheme is the same as in Figs. 2 and 3. Shaded areas represent ± 1 standard deviation around the measured averages, scaled to a 1000 deg^2 survey.

of points on the convergence map for which $\kappa \geq \kappa_{\text{th}}$, and $\partial\Sigma(\kappa_{\text{th}})$ denotes a line integral along the curve where $\kappa = \kappa_{\text{th}}$. We refer the reader to [42] for a detailed description of our measurement procedure, and reproduce in Fig. 5 the percentage difference between the MFs for a given cosmology and the fiducial model, as a function of the threshold.

The sensitivity of all three functionals at high threshold levels is similar to that of peak counts. This is expected, since at high κ_{th} values, the set of points $\kappa \geq \kappa_{\text{th}}$ increasingly coincides with the set of lensing peaks. At lower thresholds, the sensitivity of the MF is weaker, but different for each functional, suggesting that combining them should yield tighter parameter constraints.

IV. IMPACT ON PARAMETER INFERENCE

Parameter constraints are not just determined by the sensitivity of observables, but also by their (co)variances. To assess the impact of geometry and growth on inference, we estimated the confidence levels on the parameters (Ω_m , w) in two ways. First, we quantified how different each model is from the fiducial, using the $\Delta\chi^2$,

$$\Delta\chi^2 = \sum_{i,j} (\mu_i - \mu_i^{\text{fid}}) C_{ij}^{-1} (\mu_j - \mu_j^{\text{fid}}), \quad (11)$$

where μ_i is the average of an observable over the set of convergence maps for a cosmology (for instance, the binned power spectrum), μ_i^{fid} the average for the fiducial cosmology and C_{ij}^{-1} the precision matrix. For each observable we used 20 bins, either spaced logarithmically in ℓ or linearly in κ . We did not try to optimize the number of bins or their thresholds, since our purpose was to understand the effect of geometry and growth on the parameter uncertainties, not obtain accurate or optimal estimates for a specific survey.

We computed the precision matrix in the fiducial model, to be consistent with our calculated Fisher matrices (see below), and we corrected for its bias following [45]. The bias correction is very small, $\approx 2\%$, because the number of realizations used to estimate the covariance matrix ($N_r = 1024$) is large compared to the dimensionality of the data vector ($N_b = 20$). We scaled the results by the same factor as the error bars in the figures, so that their magnitude corresponds to what would be expected for a 1000 deg^2 survey, even though in the non-Gaussian regime errors may scale logarithmically rather than as the square root of the field of view [46].

The $\Delta\chi^2$ values are listed in Table II, and are overall consistent with the conclusions from the sensitivity plots in § III. The significance at which models with different w 's can be distinguished is lower than for Ω_m , due to projection effects and the worse cancellation between ge-

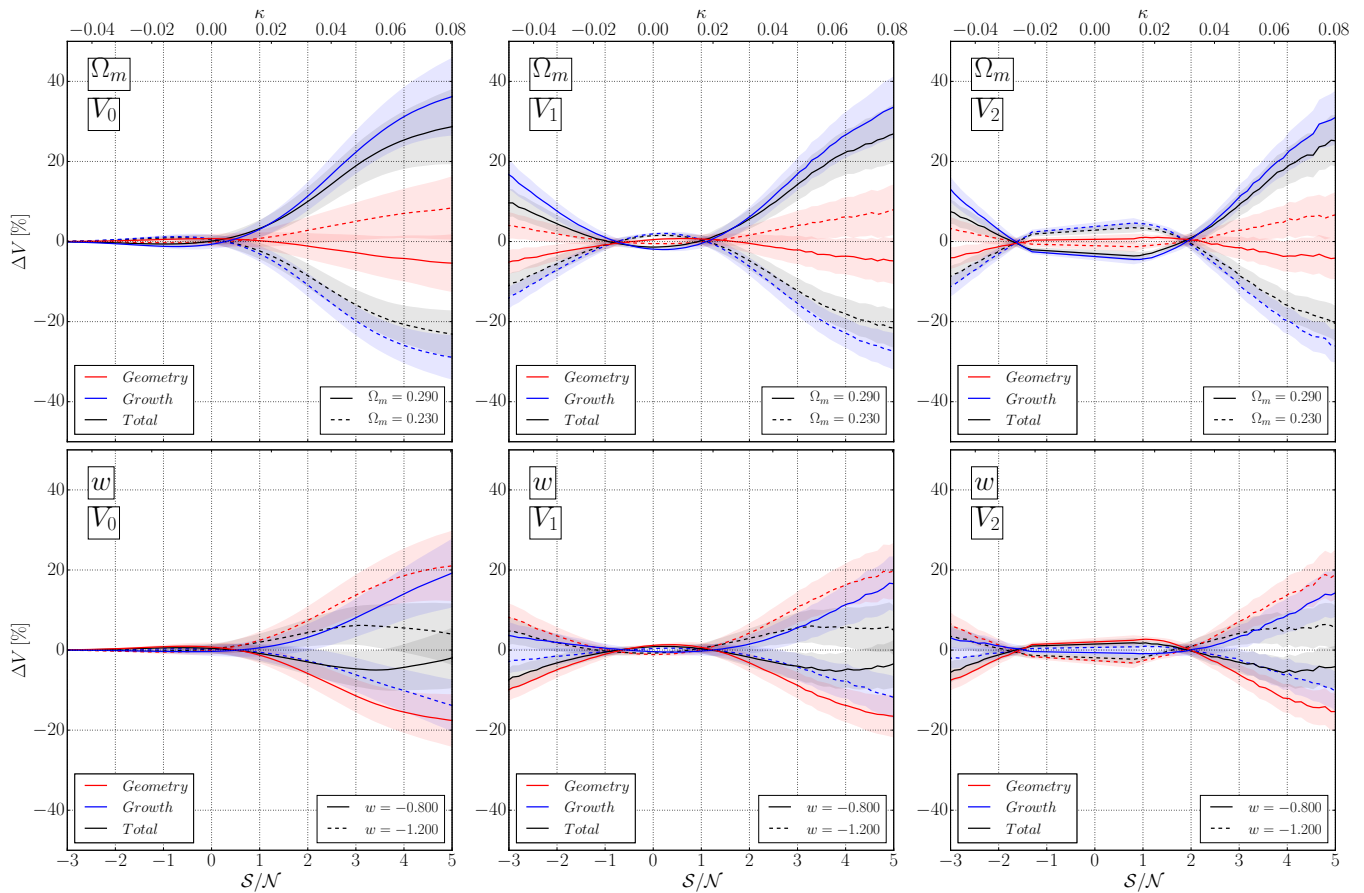


FIG. 5. (color online) Percentage difference of the three MFs measured on noisy κ maps, compared to the value in the fiducial model, when changing Ω_m and w . Left/center/right panels show the results for $V_0/V_1/V_2$, for noisy κ and source galaxies at $z_s = 1$. The color scheme, labeled in the legends, is the same as in Figs. 2-4. Shaded areas represent ± 1 standard deviation around the measured averages, scaled to a 1000 deg^2 survey.

ometry and growth. Geometry has stronger constraining power in w and growth does in Ω_m , and in general the net significance is closer to that of growth than that of geometry. The observable with the lowest $\Delta\chi^2$ is the equilateral bispectrum, especially for w , for which the cancellation between geometry and growth is particularly severe.

Even though it can strictly be used only for Gaussian-distributed data, we computed the Fisher matrix [47] for all the observables in this study, with the expectation that it provides a second-order approximation to the true parameter likelihood near its maximum:

$$F_{\alpha\beta} = \frac{1}{2} \text{Tr} [C^{-1} C_{,\alpha} C^{-1} C_{,\beta} + C^{-1} M_{\alpha\beta}], \quad (12)$$

$$M_{\alpha\beta} = \mu_{,\alpha} \mu_{,\beta}^T + \mu_{,\beta} \mu_{,\alpha}^T.$$

Here $F_{\alpha\beta}$ is one element of the Fisher matrix, Tr stands for the trace of the matrix within brackets, the covariance is evaluated at the fiducial model and a comma denotes them partial derivative $X_{,\alpha} \equiv \frac{\partial}{\partial \alpha} X$. The marginalized error on a parameter is given by $\sqrt{(F^{-1})_{\alpha\alpha}}$, and is re-

ported in Table III. We have found the finite-difference derivatives of the covariance to be sensitive to the numeric scheme used to estimate them, especially for the bispectrum. In the case of the power spectrum and peak counts, it has been shown that this does not significantly change the parameter constraints [48, 49]. For these reasons, we have not included the cosmology-dependence of the covariance in our Fisher matrix calculations. The derivatives of the average observables were estimated using 5-point finite differences with Lagrangian polynomials.

We show the 68% confidence level contours in Fig. 6. The figures show that marginalized errors on w are larger than those for Ω_m by a factor of ≈ 15 , and that geometry has less constraining power than growth. The confidence regions decrease when the sources are farther away, although the marginalized errors do not always do. This is due to changes in the degeneracies (i.e. the axes and tilt angles of the error ellipses). For example, the 68% contour from Minkowski functionals for geometry-only becomes more elongated and its tilt is increased towards

TABLE II. $\Delta\chi^2$ for different cosmological models computed for the power spectrum and three non-Gaussian observables (equilateral bispectrum, peak counts and Minkowski functionals) over noisy κ maps with source galaxies at either $z = 1$ or $z = 2$.

	Dependence on Ω_m								Dependence on w							
	0.200		0.230		0.290		0.320		-0.500		-0.800		-1.200		-1.500	
	$z = 1$	$z = 2$	$z = 1$	$z = 2$	$z = 1$	$z = 2$	$z = 1$	$z = 2$	$z = 1$	$z = 2$	$z = 1$	$z = 2$	$z = 1$	$z = 2$	$z = 1$	$z = 2$
Power spectrum																
Total	541	1550	148	421	174	444	718	1770	71	288	18	45	22	18	109	109
Geometry-only	92	670	18	142	14	101	48	375	525	2442	92	379	102	271	532	1569
Growth-only	839	3033	242	861	305	1110	1371	5083	528	3050	45	252	23	132	96	557
Equilateral bispectrum																
Total	14	38	3	13	8	8	25	41	4	5	2	3	3	4	3	5
Geometry-only	5	9	2	5	2	4	2	10	14	47	4	12	7	8	19	40
Growth-only	18	56	6	16	12	20	40	113	39	181	4	13	3	8	9	28
Peak counts																
Total	772	1120	190	266	199	232	768	825	211	399	39	48	38	26	164	93
Geometry-only	99	336	26	76	23	70	65	223	776	1934	127	253	110	178	603	837
Growth-only	1213	2431	317	588	361	542	1445	2071	321	931	40	114	20	83	117	373
Minkowski functional V_0																
Total	915	1153	231	272	212	265	859	976	413	828	64	90	52	56	268	194
Geometry-only	111	455	28	107	30	81	86	281	931	2305	150	282	126	229	711	1071
Growth-only	1464	2684	386	650	404	651	1663	2634	385	1189	38	121	26	75	116	337
Minkowski functional V_1																
Total	984	1506	245	339	229	353	901	1229	321	516	52	53	41	33	205	112
Geometry-only	118	422	27	117	29	73	88	271	996	2595	161	285	130	214	696	1075
Growth-only	1564	3313	400	799	423	753	1691	3043	635	2068	61	199	34	119	158	543
Minkowski functional V_2																
Total	1016	1862	255	438	253	446	997	1647	313	486	56	51	39	34	203	109
Geometry-only	128	602	30	141	31	101	95	375	1030	3206	173	392	145	292	764	1412
Growth-only	1613	4068	420	1000	460	997	1910	4031	736	2832	68	280	39	157	164	712

the w axis, yielding a larger marginalized error on w for $z_s = 2$ than for $z_s = 1$.

For all observables, errors on Ω_m and w are positively correlated, when either geometry or growth is considered in isolation. For example, the geometry effect of a higher matter density is smaller comoving distances, which can also be achieved with a less negative value for w . The effect on growth of a lower DE density in the past would be a smaller suppression of gravitational collapse and a stronger gravitational field for the collapsing perturbations. The correspondingly stronger lensing signal is similar to what would be achieved with higher matter density. For the net effect, the change of the dominant effect for Ω_m and w reverses the degeneracy direction, yielding anti-correlated errors on the parameters.

V. DISCUSSION

The agreement between the sensitivity to Ω_m and w of the power spectra measured on the mock κ maps and the analytic prediction, as well as the relative contribution of

geometry and growth, validates our approach based on modified simulations.

The cancelation between geometry and growth, which further suppresses the sensitivity of WL to cosmological parameters, highlights why it is important to combine different redshift bins (tomography) to constrain DE with better precision (e.g. [50]). The suppression of the power spectrum sensitivity at small scales by galaxy shape noise highlights the importance of including other observables when analyzing weak lensing data, even if non-Gaussianities were small.

The sensitivity of the equilateral bispectrum follows a similar pattern to that of the power spectrum, but their measurement is considerably noisier, which translates into a less significant $\Delta\chi^2$ for a given model. The addition of shape noise does not affect the mean sensitivity on small scales more than large scales, which is reasonable given the Gaussian noise model used (it does contribute to the statistical error).

We measured also the folded bispectrum, and the results are in line with those from the equilateral shape. We expect the same for all other configurations of the

TABLE III. Marginalized errors on Ω_m and w , orientation of the Fisher ellipse (measured as the angle between its major axis and the w axis), and figure-of-merit (FOM; defined as π/A , with A the area of the error ellipse). The errors correspond to a 68% confidence level, scaled to a 1000 deg² survey. All calculations were done on noisy κ maps with source galaxies at either $z = 1$ or $z = 2$.

	$\Delta\Omega_m$ $\times 10^3$		Δw $\times 10^3$		θ [deg]		FOM	
	$z = 1$	$z = 2$	$z = 1$	$z = 2$	$z = 1$	$z = 2$	$z = 1$	$z = 2$
Power spectrum								
Total	14.2	4.9	269.2	127.1	-2.9	-2.0	1034	3609
Geometry-only	40.7	34.4	106.6	138.3	20.3	13.9	802	1714
Growth-only	15.2	11.6	298.8	181.5	2.9	3.6	1211	3776
Equilateral bispectrum								
Total	22.3	17.0	347.2	258.4	-0.6	1.2	131	241
Geometry-only	49.4	38.2	161.1	152.9	5.9	10.2	132	239
Growth-only	34.7	34.6	396.7	326.5	4.3	5.7	142	272
Peak counts								
Total	8.9	7.3	135.9	135.9	-3.5	-2.8	2247	2538
Geometry-only	32.9	32.9	98.3	128.5	17.9	14.2	1087	1447
Growth-only	9.4	9.8	219.2	158.3	2.4	3.5	1844	3287
Minkowski functional V_0								
Total	7.6	5.1	99.8	66.4	-4.0	-3.6	3259	5387
Geometry-only	29.4	36.5	89.3	146.6	17.6	13.9	1311	1425
Growth-only	4.8	4.5	115.2	79.3	2.1	3.0	3780	7018
Minkowski functional V_1								
Total	6.1	3.2	91.0	63.9	-3.3	-1.8	3697	6355
Geometry-only	38.0	36.6	111.6	152.5	18.4	13.4	1042	1384
Growth-only	5.1	5.6	104.1	84.1	2.5	3.6	4277	7229
Minkowski functional V_2								
Total	6.5	3.1	101.2	69.9	-3.3	-1.8	3436	6579
Geometry-only	36.7	40.4	106.5	159.0	18.7	14.2	1130	1489
Growth-only	5.5	6.8	109.8	99.2	2.6	3.8	4181	6962

bispectrum, for the percentage change of the power spectrum and bispectrum does not depend on the multipole, and the cancelation between geometry and growth is a feature present at map level (see below).

The sensitivity of lensing peaks also has qualitative similarities to that of the power spectrum, but it is highly dependent on the height of the peaks. In order to assess how much of their sensitivity is a direct result of differences in the power spectrum, we computed it from Gaussian random fields (GRFs) built with the same power spectra as the κ maps generated through ray-tracing. The result of this exercise is shown in Fig. 7. We have found that the sensitivity of low peaks is reduced by a factor of ≈ 2 , and the sensitivity of the high peaks increases (although there are fewer high peaks in the GRFs). Overall, the Ω_m -sensitivity of the counts cannot be fully explained by the power spectrum.

To better understand the origin of the dependence of the peak counts' sensitivity to peak height, we look at the 3D dark matter halo counts. It is natural to compare

these quantities, since high peaks have long been known to be strongly correlated with individual high-mass DM halos hosting galaxy clusters [51–53]. The average number of halos of a given mass to a fixed redshift per solid angle can be expressed as an integral of the product of the volume element (geometry) and the halo mass function (growth).

$$\frac{dn}{d\ln M d\Omega}(M) = \int_0^{z_s} dz \frac{dV}{dz d\Omega}(z) \frac{dn}{d\ln M}(z, M) \quad (13)$$

We have computed the contribution from each effect as a function of halo mass, and displayed the results in Fig. 8. The sensitivity for halo masses above $\approx 10^{12} h^{-1} M_\odot$ tracks that of high peaks, but this is not the case for low peaks / lower mass halos. This is in agreement with previous studies that showed a link between high peaks and single high-mass halos, while finding that lower peaks are associated instead with constellations of 4-8 low-mass halos at a range of redshifts [54]; a similar peak-halo correlation has been seen in recent CFHTLens data [55].

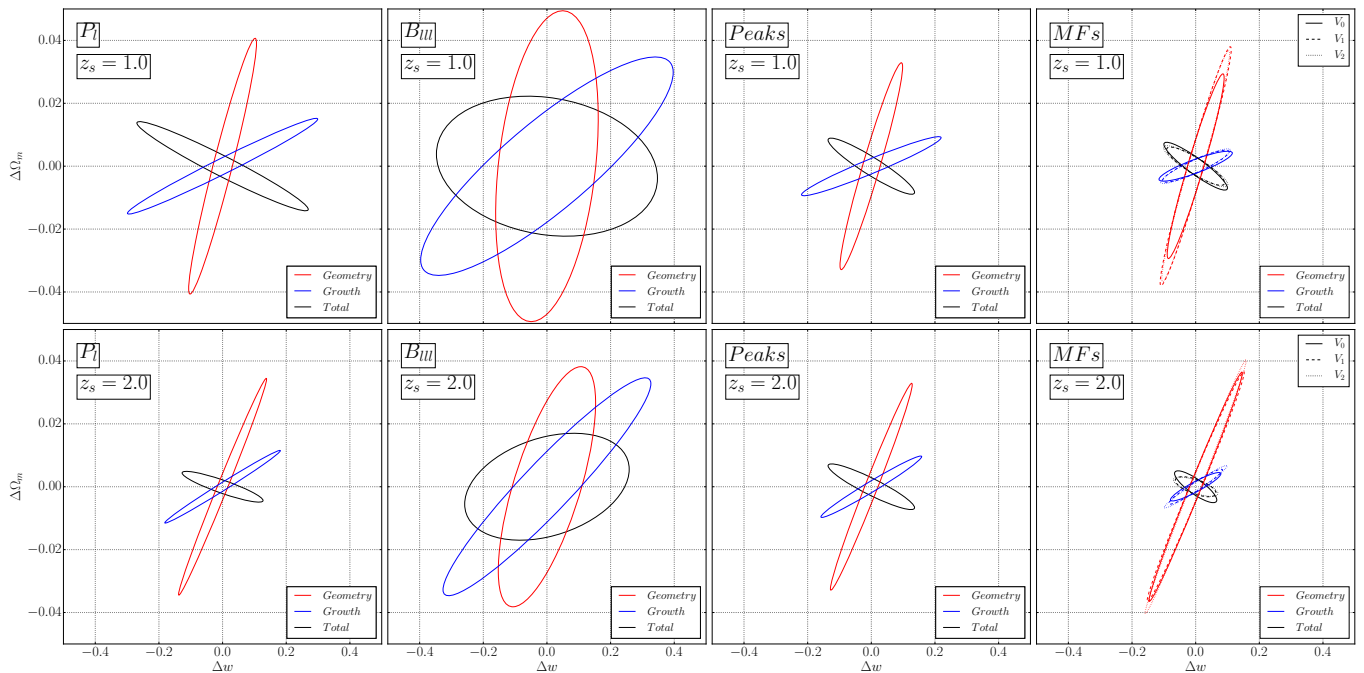


FIG. 6. (color online) 68% Fisher error ellipses in the (Ω_m, w) plane inferred from the power spectrum (P_l), equilateral bispectrum (B_{III}), lensing peaks and Minkowski functionals (MFs). Upper/lower panels show the contours for source galaxies at $z_s = 1/z_s = 2$. Each observable was characterized by a data vector of length 20, and the ellipses were computed neglecting the cosmology-dependence of the covariance matrix. All contours are scaled to a 1000 deg^2 survey.

High peaks then seem to measure, like halos, measure a combination of growth and the volume element.

The sensitivity of the low peak counts does not track that of halo counts; but these peaks are important for cosmology. When normalized by the standard deviation for the fiducial model, the difference in peak counts from the fiducial model has a maximum in the low significance region (see Fig. 9). Low peaks have also been found to contribute to cosmological parameter constraints more than high peaks, which is in agreement with previous studies [49, 54], including an analysis of peak counts in the the CFHTLenS data [38].

The sensitivity of the Minkowski functionals, as well as its decomposition into geometry and growth effects, qualitatively traces that of lensing peaks, especially at high κ levels.

Finally, the fact that we observe a partial cancellation between geometry and growth, especially when changing w , in all the statistics and topological descriptors analyzed, suggests that this property is present already at the map level. In order to investigate whether this is the case, we have examined the difference-maps between each model and the fiducial, including either the geometry or growth effect alone. These maps are shown in Fig. 10 for the model with $w = -1.2$. The modified angular positions of structures in the maps built including each effect, due to different ray deflections, prevent us from directly demonstrating a cancellation of the lensing

signal by adding these maps together. Nevertheless, the geometric and growth-induced distortions in the two panels of Fig. 10 clearly show the same structures at roughly the same locations, but with the sign of their $\Delta\kappa$ values reversed. We conclude that the geometry *vs* growth cancellation indeed is a property at the map level and we therefore expect it to affect any observable, including those not analyzed here.

VI. CONCLUSIONS

We have validated the use of N-body simulations and ray-tracing to separately study the effect of geometry and growth on weak lensing observables. This allows us to extend past analyses to non-Gaussian statistics and topological features that do not admit a simple analytic treatment.

Our analysis confirms that the sensitivity of non-Gaussian observables to cosmology shares some characteristics with that of the power spectrum. They suffer a partial cancellation between geometry and growth on top of the loss of sensitivity due to integrating (projection) effects. This cancellation is more severe for w , reducing even further the sensitivity of WL to that parameter compared to Ω_m .

Galaxy shape noise dominates the power spectrum at high multipoles, reinforcing the case to use alternative

ACKNOWLEDGMENTS

We acknowledge stimulating conversations with Lloyd Knox, which motivated this work. We thank the anonymous referee for useful comments that improved this paper. The ray-tracing simulations and parameter estimation calculations were performed at the NSF XSEDE facility, supported by grant number ACI-1053575. This work was supported in part by NSF Grant No. AST-1210877, the Research Opportunities and Approaches to Data Science (ROADS) program at the Institute for Data Sciences and Engineering at Columbia University. ZH gratefully acknowledges support by a Simons Fellowship in Theoretical Physics.

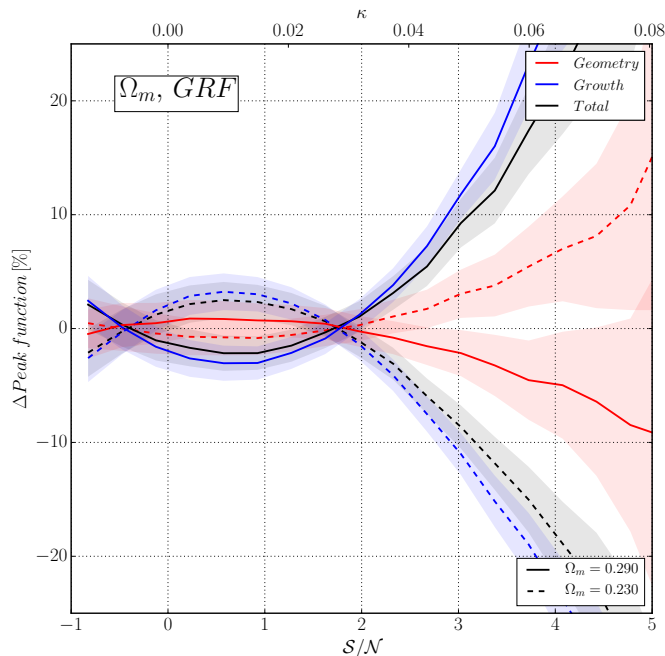


FIG. 7. (color online) *Sensitivity of lensing peak counts to Ω_m , derived from a set of Gaussian random fields with the same power spectra as that measured on noisy convergence maps from large-scale structure. Shaded areas represent 1 standard deviation errors in a 1000 deg² survey. Compare with the left panel of Fig.4*

observables to analyze weak lensing data on small scales. The bispectrum has higher statistical noise, but shape noise does not suppress its average sensitivity at high multipoles as it does for the power spectrum. The lensing peaks' sensitivity is highly dependent on the peak height, with high peaks tracking the behavior of dark matter halo counts, but low peaks having an important influence on parameter constraints. The sensitivity of Minkowski functionals is similar to that of peak counts, which is not surprising at high κ levels. The similarities between statistics, such as the cancelation of geometry and growth effects, arises from the fact that this property is present at map level.

The partial cancelation, together with projection effects, yields weak constrains for w , and underscores the need to combine information from different redshifts to tighten constrains on DE. Marginalized errors on Ω_m and w are similar to those calculated from growth-only effects. This suggests that combining WL data with probes that strongly constrain the expansion history through geometry, such as BAO measurements, may be especially beneficial to tighten constraints.

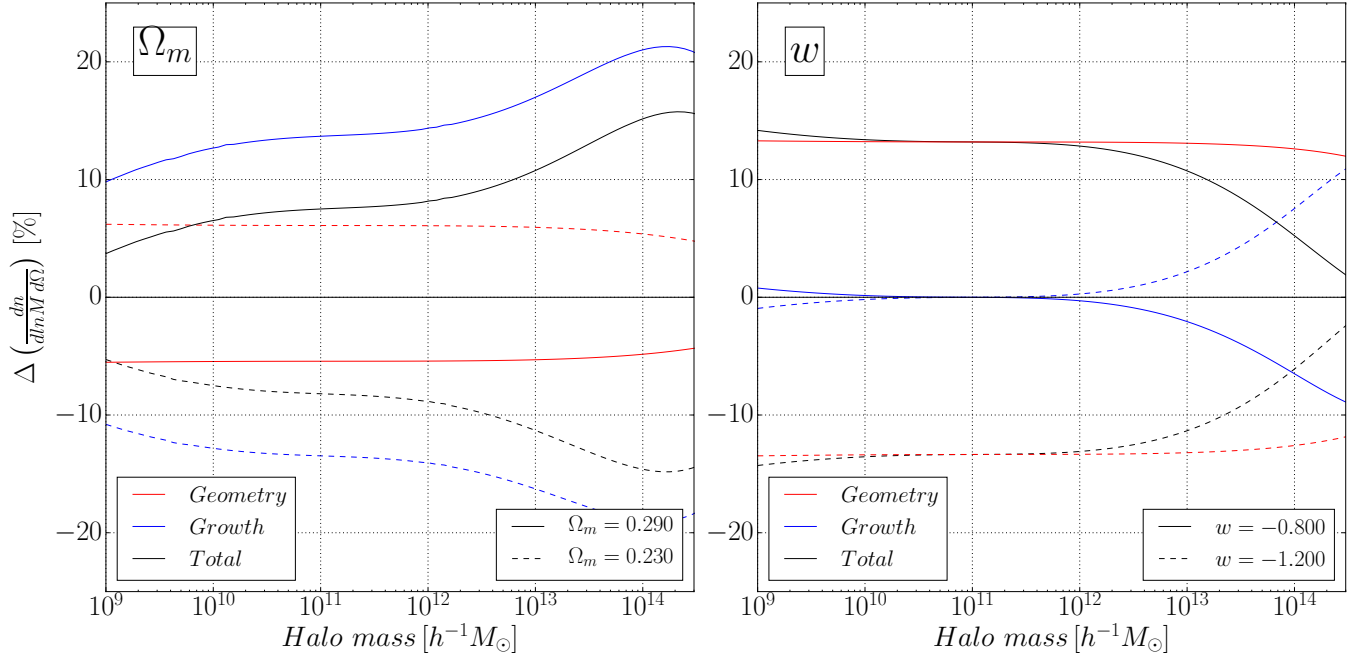


FIG. 8. (color online) Sensitivity of DM halo abundance to Ω_m (left panel) and w (right panel). The percentage difference in the total number of halos per unit solid angle to $z = 1$ between a model and the fiducial cosmology, as a function of the halo mass. The net effect (black) is decomposed into its geometry (red) and growth (blue) components.

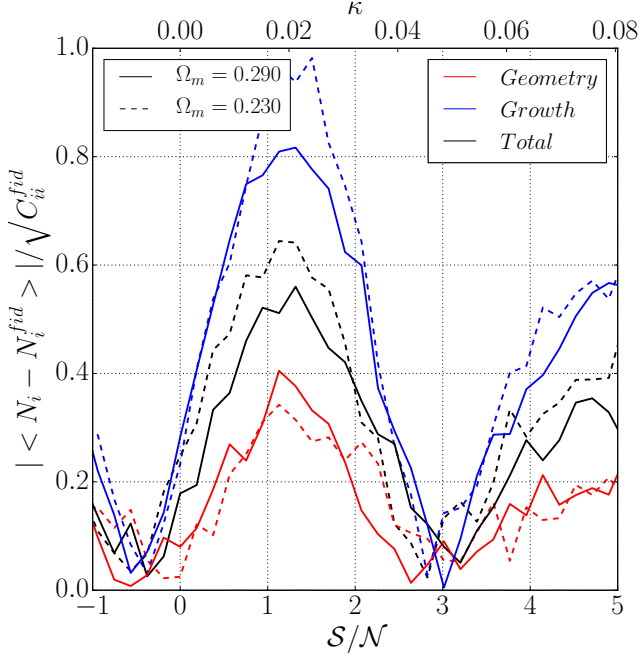


FIG. 9. (color online) *Difference in number of peaks from the fiducial cosmology, normalized by the standard deviation in the fiducial model, for a 1000 deg² survey.*

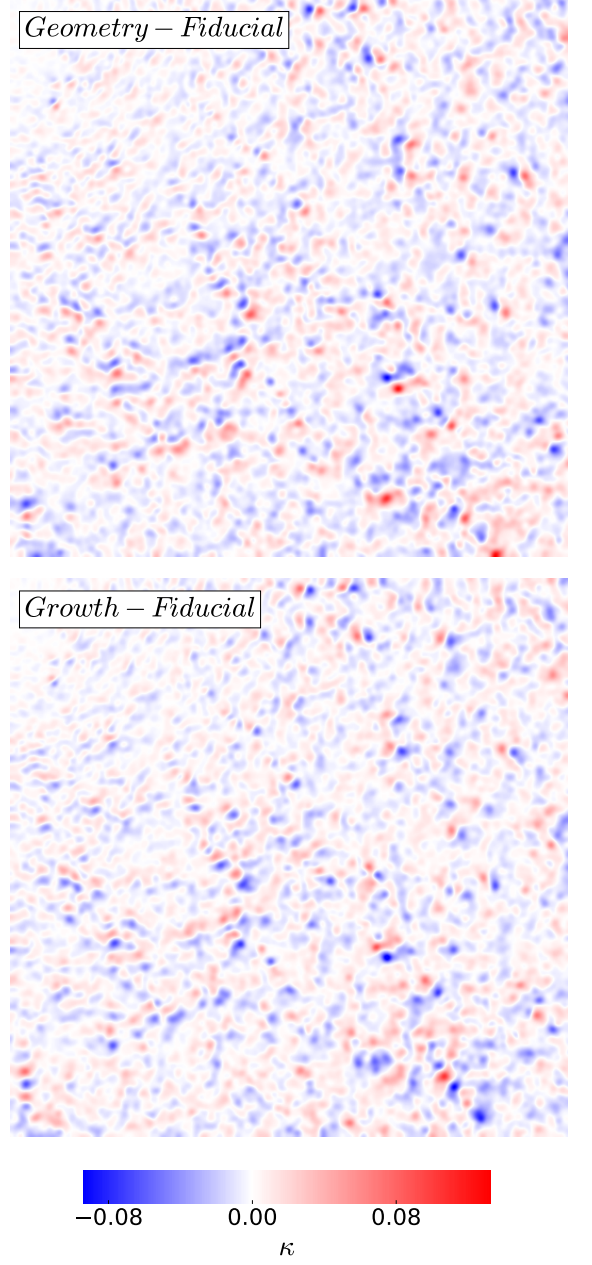


FIG. 10. (color online) *Difference $\Delta\kappa$ between a single realization of the noisy κ field generated including only geometry (top panel) or growth effects (bottom panel) for $w = -1.2$, and the corresponding realization in the fiducial model ($w = -1.0$).*

-
- [1] A. G. Riess *et al.*, *AJ* **116**, 1009 (1998), astro-ph/9805201.
- [2] S. Perlmutter *et al.*, *ApJ* **517**, 565 (1999), astro-ph/9812133.
- [3] L. Anderson *et al.*, *MNRAS* **441**, 24 (2014), arXiv:1312.4877.
- [4] R. A. Alpher, H. Bethe, and G. Gamow, *Physical Review* **73**, 803 (1948).
- [5] C. J. Copi, D. N. Schramm, and M. S. Turner, *Science* **267**, 192 (1995), astro-ph/9407006.
- [6] Planck Collaboration, P. A. R. Ade, N. Aghanim, M. Arnaud, M. Ashdown, J. Aumont, C. Baccigalupi, A. J. Banday, R. B. Barreiro, J. G. Bartlett, and et al., *A&A* **594**, A13 (2016), arXiv:1502.01589.
- [7] M. Fukugita and P. J. E. Peebles, *ApJ* **616**, 643 (2004), astro-ph/0406095.
- [8] M. Bartelmann and P. Schneider, *Phys. Rep.* **340**, 291 (2001), astro-ph/9912508.
- [9] M. Kilbinger, *Reports on Progress in Physics* **78**, 086901 (2015), arXiv:1411.0115.
- [10] <http://www.darkenergysurvey.org>.
- [11] <http://www.lsst.org>.
- [12] <http://sci.esa.int/Euclid/>.
- [13] wfirst.gsfc.nasa.gov.
- [14] F. Bernardeau, L. van Waerbeke, and Y. Mellier, *A&A* **322**, 1 (1997), astro-ph/9609122.
- [15] L. Hui, *ApJ* **519**, L9 (1999), astro-ph/9902275.
- [16] D. Munshi and B. Jain, *MNRAS* **322**, 107 (2001), astro-ph/9912330.
- [17] B. Jain and L. Van Waerbeke, *ApJ* **530**, L1 (2000), astro-ph/9910459.
- [18] J. Sato, M. Takada, Y. P. Jing, and T. Futamase, *ApJ* **551**, L5 (2001), astro-ph/0104015.
- [19] F. Simpson and S. Bridle, *Phys. Rev. D* **71**, 083501 (2005), astro-ph/0411673.
- [20] H. Zhan, L. Knox, and J. A. Tyson, *ApJ* **690**, 923 (2009), arXiv:0806.0937.
- [21] B. Jain and A. Taylor, *Physical Review Letters* **91**, 141302 (2003), astro-ph/0306046.
- [22] J. Zhang, L. Hui, and A. Stebbins, *ApJ* **635**, 806 (2005), astro-ph/0312348.
- [23] S. Wang, L. Hui, M. May, and Z. Haiman, *Phys. Rev. D* **76**, 063503 (2007), arXiv:0705.0165.
- [24] E. J. Ruiz and D. Huterer, *Phys. Rev. D* **91**, 063009 (2015), arXiv:1410.5832.
- [25] E. Krause and C. M. Hirata, *A&A* **523**, A28 (2010), arXiv:0910.3786.
- [26] S. Dodelson and P. Zhang, *Phys. Rev. D* **72**, 083001 (2005), astro-ph/0501063.
- [27] A. Petri, Z. Haiman, and M. May, *ArXiv e-prints* (2016), arXiv:1612.00852.
- [28] A. Petri, *Astronomy and Computing* **17**, 73 (2016), arXiv:1606.01903.
- [29] V. Springel, *MNRAS* **364**, 1105 (2005), astro-ph/0505010.
- [30] A. Petri, Z. Haiman, and M. May, *Phys. Rev. D* **93**, 063524 (2016), arXiv:1601.06792.
- [31] R. E. Smith *et al.*, *MNRAS* **341**, 1311 (2003), astro-ph/0207664.
- [32] L. van Waerbeke, *MNRAS* **313**, 524 (2000), astro-ph/9909160.
- [33] P. Schneider, L. van Waerbeke, B. Jain, and G. Kruse, *MNRAS* **296**, 873 (1998), astro-ph/9708143.
- [34] F. Bernardeau, Y. Mellier, and L. van Waerbeke, *A&A* **389**, L28 (2002), astro-ph/0201032.
- [35] L. Fu *et al.*, *MNRAS* **441**, 2725 (2014), arXiv:1404.5469.
- [36] J. M. Kratochvil, Z. Haiman, and M. May, *Phys. Rev. D* **81**, 043519 (2010), arXiv:0907.0486 [astro-ph.CO].
- [37] J. P. Dietrich and J. Hartlap, *MNRAS* **402**, 1049 (2010), arXiv:0906.3512.
- [38] J. Liu, A. Petri, Z. Haiman, L. Hui, J. M. Kratochvil, and M. May, *Phys. Rev. D* **91**, 063507 (2015), arXiv:1412.0757.
- [39] X. Liu, C. Pan, R. Li, H. Shan, Q. Wang, L. Fu, Z. Fan, J.-P. Kneib, A. Leauthaud, L. Van Waerbeke, M. Makler, B. Moraes, T. Erben, and A. Charbonnier, *MNRAS* **450**, 2888 (2015), arXiv:1412.3683.
- [40] T. Kacprzak *et al.*, *MNRAS* **463**, 3653 (2016), arXiv:1603.05040.
- [41] K. R. Mecke, T. Buchert, and H. Wagner, *A&A* **288**, 697 (1994), astro-ph/9312028.
- [42] J. M. Kratochvil, E. A. Lim, S. Wang, Z. Haiman, M. May, and K. Huffenberger, *Phys. Rev. D* **85**, 103513 (2012), arXiv:1109.6334 [astro-ph.CO].
- [43] M. Shirasaki and N. Yoshida, *ApJ* **786**, 43 (2014), arXiv:1312.5032.
- [44] A. Petri, J. Liu, Z. Haiman, M. May, L. Hui, and J. M. Kratochvil, *Phys. Rev. D* **91**, 103511 (2015), arXiv:1503.06214.
- [45] J. Hartlap, P. Simon, and P. Schneider, *A&A* **464**, 399 (2007), astro-ph/0608064.
- [46] P. Creminelli, L. Senatore, and M. Zaldarriaga, *J. Cosmology Astropart. Phys.* **3**, 019 (2007), astro-ph/0606001.
- [47] M. Tegmark, A. N. Taylor, and A. F. Heavens, *ApJ* **480**, 22 (1997), astro-ph/9603021.
- [48] C.-A. Lin and M. Kilbinger, *A&A* **583**, A70 (2015), arXiv:1506.01076.
- [49] J. M. Zorrilla Matilla, Z. Haiman, D. Hsu, A. Gupta, and A. Petri, *Phys. Rev. D* **94**, 083506 (2016), arXiv:1609.03973.
- [50] W. Hu, *ApJ* **522**, L21 (1999), astro-ph/9904153.
- [51] M. White, L. van Waerbeke, and J. Mackey, *ApJ* **575**, 640 (2002), arXiv:astro-ph/0111490.
- [52] T. Hamana, M. Takada, and N. Yoshida, *MNRAS* **350**, 893 (2004), arXiv:astro-ph/0310607.
- [53] J. F. Hennawi and D. N. Spergel, *ApJ* **624**, 59 (2005), arXiv:astro-ph/0404349.
- [54] X. Yang, J. M. Kratochvil, S. Wang, E. A. Lim, Z. Haiman, and M. May, *Phys. Rev. D* **84**, 043529 (2011), arXiv:1109.6333.
- [55] J. Liu and Z. Haiman, *Phys. Rev. D* **94**, 043533 (2016), arXiv:1606.01318.